Transport of photoelectrons in the nightside magnetosphere

G. V. Khazanov
National Space Science and Technology Center, NASA Marshall Space Flight Center, Huntsville, Alabama, USA

M. W. Liemohn
Space Physics Research Laboratory, University of Michigan, Ann Arbor, USA

Received 11 June 2001; revised 15 October 2001; accepted 16 October 2001; published 31 May 2002.

[1] Kinetic modeling results are analyzed to examine the transport of photoelectrons through the nightside inner magnetosphere. Two sources are considered, those on the dayside from direct solar illumination and those across the nightside from light scattered by the upper atmosphere and geocorona. A natural filter exists on the nightside for the dayside photoelectrons. Coulomb collisions erode the distribution at low energies and low L shells, and magnetospheric convection compresses the electrons as they drift toward dawn. It is shown that for low-activity levels a band of photoelectrons forms between $L = 4$ and 6 that extends throughout the nightside local times and into the morning sector. For the scattered light photoelectrons the trapped zone throughout the nightside is populated with electrons of $E < 30$ eV. At high L shells near dawn, convective compression on the nightside yields an accelerated population with electrons at energies up to twice the ionospheric energy maximum (that is, roughly 1200 eV for dayside photoelectrons and 60 eV for scattered light electrons). Modeled energy and pitch angle distributions are presented to show the features of these populations. *INDEX TERMS:* 2736 Magnetospheric Physics: Magnetosphere/ionosphere interactions; 7807 Space Plasma Physics: Charged particle motion and acceleration; 2753 Magnetospheric Physics: Numerical modeling; 2730 Magnetospheric Physics: Magnetosphere—inner; *KEYWORDS:* superthermal electrons, inner magnetosphere, plasmasphere, numerical modeling, convection

1. Introduction

[2] After escaping from the upper atmosphere along the field line and then being scattered into the geomagnetic trap [e.g., *Mantas et al.*, 1978; *Lejeune*, 1979; *Polyakov et al.*, 1979; *Khazanov et al.*, 1992, 1993, 1994; *Khazanov and Gefan*, 1982], photoelectrons created in the dayside ionosphere can be transported into and through the nightside inner magnetosphere [*Khazanov et al.*, 1996, 1998]. A corotating flux tube experiences a continuous source of photoelectrons in the 1–500 eV range from the ionosphere in the daytime. During this period (12 out of every 24 hours) the trapped zone is filled to equilibrium with these particles. Once the source turns off at dusk, there is a distinctive timescale for the decay of the intensity of these electrons. Depending on the thermal plasma density and convection strength, some of these electrons will not be lost into the nightside ionosphere but rather will be transported into the dawn sector. This creates an anomalous enhancement in the dayside photoelectron distribution, particularly at high values of L (near the quiet time plasmapause), pitch angle, and energy.

[3] This scenario is most prominent during extended periods of low geomagnetic activity. During high activity the cross-tail convection electric field convects the photoelectrons in the afternoon sector sunward toward the magnetopause, and only the innermost L shells have dayside photoelectrons moving through the nightside. However, at these L shells the plasmaspheric density is large and the photoelectrons are quickly eroded from the trapped zone. During quiet times the photoelectrons on the nightside at small L values are still eroded away. However, on the L shells just inside the Alfvén boundary the photoelectrons can survive the transit through the nightside magnetosphere. This channel of photoelectrons heats the thermal electron population, offering a significant source of energy to the core plasma at this location at these times [*Khazanov et al.*, 1998, 2000].

[4] Also discussed in the studies of *Liemohn et al.* [1998] and *Khazanov et al.* [1998] is the distribution of plasma sheet electrons impinging into the inner magnetosphere. These create a trapped population at higher energies (a few hundred eV and up) that can last for days. These electrons, however, are rather inefficient at heating the thermal plasma. Low-energy photoelectrons are far more efficient at this task. A source of nightside low-energy electrons has not been studied extensively and certainly not their transport through the inner magnetosphere. The only plausible source is photoelectrons created by light scattered by the upper atmosphere and geocorona [e.g., *Strobel et al.*, 1974]. These photoelectrons are created not only on the dayside but also throughout the nightside ionosphere.

[5] It is the purpose of this study to show the magnetospheric distribution of these photoelectrons, from both the dayside and scattered light sources, throughout the nightside inner magnetosphere. The focus will be on geomagnetically quiet times, because this is when these populations are most prominent in this region. While the propagation of photoelectrons through the nightside magnetosphere was originally presented by *Khazanov et al.* [1996, 1998], they only discussed the 90° equatorial pitch angle distribution from the dayside source. Upon investigating the nightside source and examining the full velocity space distribution, remarkable pitch angle dependencies were found, and so a more detailed presentation of our previous results is given below in addition to the new results from the scattered light photoelectron source. To the authors' knowledge, no published study of nightside magnetospheric photoelectron observations exists. The present study presents and discusses the theoretical prediction of unique velocity space distributions arising from nightside electron trans-

0148-0227/02/2001JA000163$09.00

port, and it is left as a future investigation to provide observational confirmation.

2. Technique

[6] Like other charged particles, the motion of photoelectrons through near-Earth space can be categorized by several timescales. The first is the gyroperiod of the electrons in the presence of the geomagnetic field. This timescale is very fast (microseconds), and, because the source is assumed to be isotropic, can be averaged out of the transport equations. The next timescale is the bounce period, the time needed for an electron to traverse the length of the field line to the conjugate ionosphere (or mirror point) and back again. Depending on the latitude (L shell) and the energy of the photoelectron, this timescale is of the order of seconds to minutes. Resolving this motion is important when examining the interhemispheric transport of these electrons. Another timescale of interest is the one relating to collisional scattering. In the ionosphere the collisional timescales are much less than a second. Out along the field line, particularly at the top of the field line where it crosses the equatorial plane, the timescales are far slower, taking hours to fill the trapped zone of velocity space through Coulomb scattering. Similarly, convective and corotational drifts of photoelectrons in the inner magnetosphere have timescales of the order of hours. Therefore, if these relatively slow processes are the ones of interest, then resolving the details of the faster processes, such as those in the ionosphere or the interhemispheric transport of these particles, is unnecessarily burdensome.

2.1. Model Description

[7] The two magnetospheric photoelectron timescale regimes (the fast, collisionless, interhemispheric motion to fill the fly through zone and the slow pitch angle scattering and cross-field drift to fill the rest of phase space) are best handled with two separate transport models. Therefore two models of superthermal electron transport are used in this study. The first is one that calculates the velocity space distribution everywhere along a flux tube, from the bottom of the ionosphere in one hemisphere up through the plasmasphere and down to the bottom of the conjugate ionosphere [*Khazanov and Liemohn*, 1995; *Liemohn et al.*, 1997a],

$$\frac{\beta}{\sqrt{E}}\frac{\partial\phi}{\partial t}+\mu\frac{\partial\phi}{\partial s}-\frac{1-\mu^2}{2}\left(\frac{1}{B}\frac{\partial B}{\partial s}-\frac{F}{E}\right)\frac{\partial\phi}{\partial\mu}+EF\mu\frac{\partial}{\partial E}\left(\frac{\phi}{E}\right)=Q+\overline{S}, \tag{1}$$

which solves for the differential number flux distribution ϕ in gyration-averaged phase space along a single flux tube (with independent variables of time t, distance along the field line s, electron kinetic energy E, and cosine of the local pitch angle μ = cos α). The inhomogeneity of the geomagnetic field is included ($\partial B/\partial s$), as well as other forces, such as electric fields, in F. The primary source distribution enters the equation through Q, and this is calculated from two illumination sources: direct solar illumination and scattered light illumination. Elastic and inelastic scattering processes with the neutral particles of the upper atmosphere as well as with the thermal plasma electrons and ions are included along the entire flux tube, represented by the $\overline{S}$ term in equation (1). The details of the chosen description of $\overline{S}$ can be found in the works of *Khazanov et al.* [1994] and *Khazanov and Gefan* [1982]. Note that $\overline{S}$ includes the production of secondary electrons (and tertiary, and so on) in the upper atmosphere, and therefore the resulting distributions are not simply the primary electrons but actually represent a total electron spectra. The terms "photoelectron" and "scattered light" will be used in the text below to identify the total electron distributions created by the two illumination sources considered in this study.

[8] The second model averages over the motion along the field line and instead includes the motion of the particles across field lines [e.g., *Khazanov et al.*, 1996],

$$\frac{\partial\langle f\rangle}{\partial t}+\langle\mathbf{V}_D\rangle\frac{\partial\langle f\rangle}{\partial\mathbf{R}_\perp}+\left\langle\frac{dE}{dt}\right\rangle\frac{\partial\langle f\rangle}{\partial E}+\left\langle\frac{d\mu_0}{dt}\right\rangle\frac{\partial\langle f\rangle}{\partial\mu_0}=\left\langle\frac{\delta f}{\delta t}\right\rangle_{CC}-\frac{\langle f\rangle}{0.5\tau_b}, \tag{2}$$

which solves for the photoelectron phase space density f (where $f = m^2\phi/2E$) in the equatorial plane. The equation is solved in the magnetic equatorial plane, with position given by $\mathbf{R}_\perp$. The distribution is assumed to be uniform along the field line for a given equatorial pitch angle (an adiabatic invariant of the bounce motion), and therefore the distribution at any point in the inner magnetosphere can be known simply by mapping the equatorial velocity space distribution along the field line to the location of interest. The pitch angle at some point along the field line is related to its equatorial value (μ_0) by the formula

$$\mu=\pm\sqrt{1-\frac{B(s)}{B_0}\left(1-\mu_0^2\right)}\ . \tag{3}$$

Also included in this calculation are Coulomb collisions (energy degradation and pitch angle scattering) with the thermal plasma in the inner magnetosphere (the "cc" collision term in equation (2)) as well as precipitation into the atmosphere (on a timescale of half a bounce period τ_B), applied only to pitch angles that map to the ionosphere. *Khazanov et al.* [1998] showed that equation (2) is valid for electrons down to a few eV in energy, which is usually the energy of the thermal-superthermal transition. This code has been used extensively for superthermal electron transport in the inner magnetosphere [*Khazanov et al.*, 1996, 1998, 2000; *Liemohn et al.*, 1998].

[9] A combined model that couples these two transport codes can therefore handle the entire three-dimensional flow of photoelectrons in the subauroral ($L \leq 7$) ionosphere and magnetosphere, resolving timescales from less than a second up to days. The details of this coupling procedure and initial results are discussed by *Khazanov et al.* [1998]. It is useful to mention here that the standard solution algorithm uses the single flux tube model inside the fly through zone of velocity space (that is, the source/loss cone, depending on local time) and the bounce-averaged model in the trapped zone of velocity space (those equatorial pitch angles that do not map to the ionosphere). The loss cone boundary is therefore an interface between the two models. This is the equatorial pitch angle that mirrors at the top of the ionosphere, taken at 800-km altitude in this study,

$$\mu_{0,\mathrm{LCB}}=\sqrt{1-\frac{B_0}{B_{800}}} \tag{4}$$

(loss cone boundary (LCB) is used because this is the conventional terminology for this pitch angle). The value of $\mu_{0,\mathrm{LCB}}$ varies with L shell, of course, ranging from 0.94 ($\alpha_{0,\mathrm{LCB}} = 20°$) at $L = 2$ to 0.9985 ($\alpha_{0,\mathrm{LCB}} = 3°$) at $L = 6.5$, assuming a dipole geomagnetic field. There are only two processes that transfer electrons between the model domains (that is, across $\mu_{0,\mathrm{LCB}}$): Coulomb collisions with the magnetospheric thermal plasma and cross-L drift (through adiabatic invariant conservation).

[10] These models have been tested for validity against other observational data as well as other simulation algorithms. For the single-flux tube model, *Khazanov and Liemohn* [1995, 1998] show good comparison with data from the Atmospheric Explorer E and Dynamics Explorer 1 and 2 (DE 1 and 2) satellites.

Liemohn and Khazanov [1995] discuss the energy conservation of the numerical scheme, and *Khazanov and Liemohn* [1998] show direct comparisons against two-stream and particle-tracking photoelectron transport codes. The bounce-averaged code was compared against electron data from the Combined Release and Radiation Effects Satellite (CRRES) by *Liemohn et al.* [1998], and the ion version of this algorithm has been successfully compared against ring current data many times [e.g., *Fok et al.*, 1995; *Jordanova et al.*, 1998; *Liemohn et al.*, 2001]. The energy conservation of this code was shown to be excellent [*Fok et al.*, 1993; *Liemohn et al.*, 1999]. In the present study, data comparisons are not included because this is out of scope. The focus is on showing the theoretical prediction of peculiar features of the electron distribution in the inner magnetosphere and to understand the governing physical mechanisms.

[11] In the results below, the focus is on the effects of transport on the electrons as they move through the nightside magnetosphere. Of particular interest are the unique velocity space distributions arising from the motion-induced energization. Wave excitation and wave-particle interactions have been omitted from the calculation in order to concentrate on the interplay between the convective processes. Plasma instabilities and wave interaction effects will be examined in the future. A comparison with the diffusion timescales calculated by *Liemohn et al.* [1997b] shows that the photoelectron energy range ($E < 1$ keV) is not significantly affected by plasmaspheric hiss, except in regions of strong density gradients where the waves can become guided.

2.2. Model Input and Boundary Information

[12] For the simulation results presented below, input and boundary information is needed for each of the models. For the single-flux tube model, dayside solar EUV and X ray radiation spectra were obtained using the *Hinteregger et al.* [1981] model, while the scattered light photon source was taken from *Strobel et al.* [1974]. The neutral thermospheric densities and temperatures were given by mass spectrometer incoherent scatter 1990 (MSIS-90) [*Hedin*, 1991], and the background ionosphere was calculated based on the international reference ionosphere (IRI) model [*Bilitza*, 1990]. Photoabsorption and photoionization cross sections for O, O_2, and N_2 were taken from *Fennelly and Torr* [1992]. Partial photoionization cross sections for O_2 and N_2 were obtained from *Conway* [1988], while partial photoionization cross sections of *Bell and Stafford* [1992] were adopted for atomic oxygen. Cross sections for elastic collisions, state-specific excitation, and ionization were taken from *Solomon et al.* [1988].

[13] In the bounce-averaged electron transport model a shielded Volland-Stern convection pattern [*Volland*, 1973; *Stern*, 1975] is used with a very low activity coefficient ($Kp = 1$ in a *Maynard and Chen* [1975] intensity formula). This field is held constant, and the calculations are conducted until a steady state solution is obtained everywhere within the simulation domain (up to 48 hours of simulation time). The model also uses a dipole magnetic field (particularly valid during quiet times) and a *Rasmussen et al.* [1993] dynamic plasmasphere model for the thermal core population. The initial condition is taken as zero everywhere, with a boundary condition (from the single flux tube model) at the edge of the loss cone. Particles are lost if they drift across the inner L shell boundary (last cell is centered at $L = 2.0$), while drift across the outer boundary (last cell centered at $L = 6.5$) is handled according to the method described by *Liemohn et al.* [1998]. This algorithm takes into account the open-closed drift path boundary and assigns either zero flux for an open trajectory or the flux from an earlier local time for a closed trajectory.

[14] The contributions to the velocity space distribution for each source (direct solar illumination and scattered light illumination, including all secondary electrons) will be identified and discussed, first separately and then as a combined source. These results will also be compared against plasma sheet electron flux levels using the results from *Khazanov et al.* [1998].

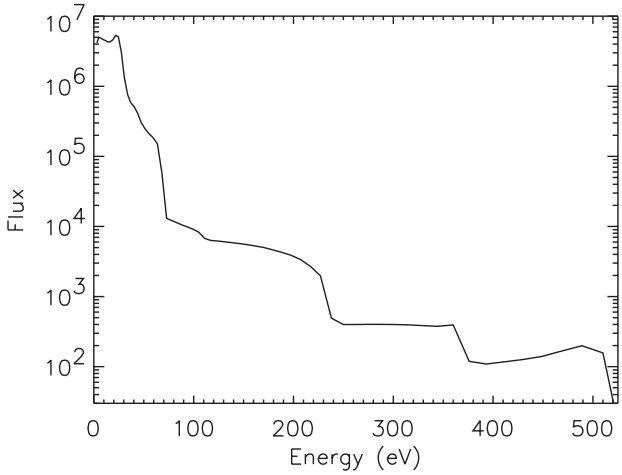

Figure 1. Typical dayside photoelectron source cone distribution produced by the single flux tube model for use as a boundary condition in the bounce-averaged model. The units are those of differential number flux, eV^{-1} cm^{-2} s^{-1} sr^{-1}, here and throughout the rest of the paper.

3. Results

[15] All of the results shown here are from simulations conducted out to steady state. It should be noted that each spatial location requires a different time to reach this equilibrium level for each source population. For instance, the nightside features from the dayside photoelectron source will develop within 12 hours, but the resulting morningside features take up to 24 hours to form and some of the outer L shell features can take 48 hours to fully mature. Similarly, the scattered light source distributions deep within the plasmasphere take only a few hours to reach a steady flux level at all pitch angles and energies, but the nonlocal convective features from this source population (again, in the outer L shells) take more than a day to fully develop.

3.1. Dayside Photoelectron Source

[16] The single flux tube model solves for the velocity space distribution everywhere along a field line. To couple with the bounce-averaged code, only a single energy spectrum is needed for each latitude and longitude location. Therefore the boundary condition that is passed from the single flux tube model to the bounce-averaged code is a field line averaged flux spectrum at the loss cone boundary. Figure 1 shows a typical energy spectrum at the source cone boundary for the dayside photoelectron source population. It is very similar to the "typical spectrum" shown in our previous work [*Khazanov et al.*, 1998], but it (along with all of the other simulation results for the dayside photoelectron source) has been recalculated with the latest versions of the models. Note that many of the photoelectron energy spectrum features that are spiky at lower altitudes (deep in the ionosphere), particularly ionization peaks created by distinct spectral lines in the solar photon source, are smoothed away in this spectrum due to collisions with the upper atmospheric neutral particles and the ionospheric and plasmaspheric thermal plasma core populations. The very low energy range below 5 eV is sloped upward owing to Coulomb collisional damping by the thermal plasma, and the production peaks in the 20–30 eV range are essentially washed out into a single hump in the spectrum (due to collisions and energy grid resolution). The sharp drops near 70 and 220 eV are

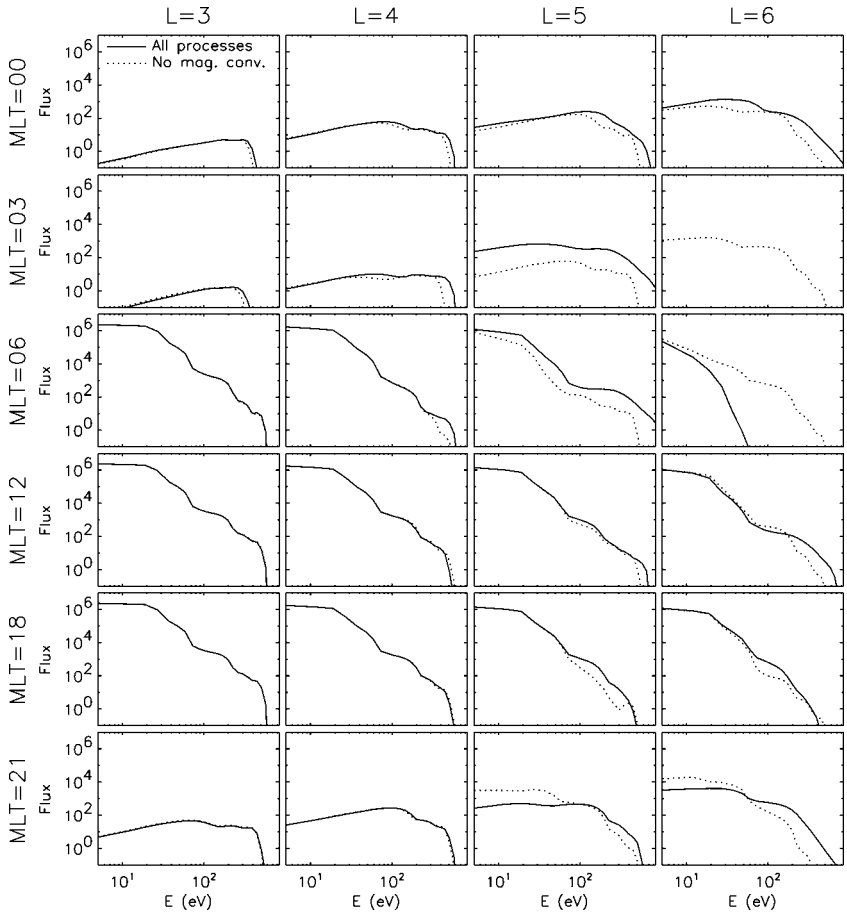

Figure 2. Dayside photoelectron source energy spectra at 20° equatorial pitch angle at various locations throughout the simulation domain. The rows are at MLT = 0000, 0300, 0600, 1200, 1800, and 2100 and the columns are at L = 3, 4, 5, and 6. The solid line is the solution with all processes included, while the dotted line is the solution with the magnetospheric convection electric field set to zero.

from corresponding decreases in the solar photon spectrum. The peaks near 360 and 500 eV are the Auger electron peaks created when a soft X ray removes an electron from the inner shell of an atmospheric neutral particle. Specifically, N_2 Auger electrons form a series of peaks from 315 to 367 eV, atomic oxygen forms Auger peaks from 474 to 509 eV, and the O_2 Auger electron peaks range from 456 to 507 eV (according to the solar spectrum and cross sections used in these calculations). As with the low-energy production peaks, all features of these spectra are smoothed away in this field line averaged energy spectrum. Distributions such as this are calculated from the single flux tube transport model for each spatial location and applied throughout the dayside.

[17] The source cone energy spectra supply photoelectrons to the dayside magnetosphere through scattering into the trapped zone. The resulting electron fluxes from the bounce-averaged model yield many distinctive features (to be discussed below), but the most obvious one is a band of electrons throughout the nightside in the outer plasmasphere. Figure 2 shows energy spectra in the trapped zone at various locations in the simulation domain. The band is the relatively large fluxes at high L shell (compared to the fluxes at lower L shells) across the night sector. This effect was originally presented by *Khazanov et al.* [1996, 1998], but they only discussed the 90° equatorial pitch angle distribution from the dayside source. Upon investigating the nightside source and examining the full velocity space distribution, remarkable pitch angle dependencies were found, and so a more detailed presentation of our previous results is being given. All of these spectra are at 20° equatorial pitch angle, which is in the trapped zone for all of the L shells presented in this figure. While all other trapped zone pitch angles have distinct features (which will be discussed below), only this one will be shown in line plot format for illustrative purposes.

[18] Because these simulation results are in the inner magnetosphere during quiet times, one might conclude that corotation is all that is needed to create this band of photoelectrons throughout the nightside magnetosphere. However, that is not entirely the case, and the small influence of the weak convection electric field is very important in elevating the flux levels of the photoelectrons not only on the nightside but also on the dayside. To illustrate the role of magnetospheric convection, results from two simulations are plotted in Figure 2: one that includes all drift and collisional processes (solid lines) and another that includes all processes except magnetospheric convection (dotted lines). This comparison highlights the unique situation arising from the existence of a weak (but nonzero) cross-tail electric field. The convection electric field is very important to the formation of the energized band of photoelectrons in the nightside magnetosphere, and results with only corotation can be different by several orders of magnitude.

[19] Since the spectra in Figure 2 are taken from within the trapped zone, some process had to move these electrons into this region of velocity space. Collisional scattering from the source cone is the primary mechanism for this motion on the dayside (flux tube expansion is another). Because Coulomb collisions with the thermal plasma are dependent on the energy of the superthermal electron (increasing efficiency with decreasing energy), the low-energy portion of the spectrum is filled in more rapidly than the

high-energy part. This is seen in Figure 2 as both simulation results have large flux values below 100 eV on the dayside. It is seen, however, that at most locations on the dayside there are more electrons present at this equatorial pitch angle (20°) when convection is included (except MLT = 0600, L = 6, to be discussed below). In addition, the spectra sometimes have substantial flux levels at energies above 509 eV, the highest Auger electron energy peak from oxygen (at MLT = 0600, L = 5 for instance), a range where there is no source population. Such fluxes are entirely due to the convection electric field compressing and expanding the flux tubes as they corotate with the Earth. Compression on the nightside allows for the energization of electrons, which not only shifts them in phase space but also reduces the influence of collisional scattering and loss. Therefore photoelectrons are able to exist throughout the nightside magnetosphere, especially the high-energy tail (compare the flux drop at 10 eV to that at 100 eV as the electrons move from MLT = 1800 to 2100). This energization (up to 1200 eV, more than twice their initial energy) is not fully compensated by dayside expansion until the dusk region (examine the L = 5 and 6 columns). Expansion on the dayside also allows for more efficient filling of the trapped zone at higher L shells (electrons are pitch angle scattered at smaller L shells and then convected outward). All of this is true even at this equatorial pitch angle, which is not particularly deep into the trapped zone.

[20] Another effect of the spatial focusing on the nightside is seen in the MLT = 0300 and 0600 results at L = 6. The simulation with magnetospheric convection included has fluxes below the scale of the plot in the MLT = 0300, L = 6 panel, and the fluxes are much smaller for this run compared to the simulation without convection in the MLT = 0600, L = 6 panel. Convection shifts the drift trajectories of the electrons inward on the nightside, and L = 6 at these locations is beyond the Alfvén boundary for electrons in this energy range.

[21] This shift is understood by considering the Alfvén boundaries for the population being examined here. This boundary separates the closed drift paths that encircle the Earth (inside the boundary) from the open drift paths that sweep particles in from the nightside and out through the dayside magnetopause (outside the boundary). By numerically determining the stagnation point and then solving the system of equations consisting of the bounce-averaged drift velocities ($\langle dR/dt\rangle$, $\langle d\varphi/dt\rangle$, $\langle dE/dt\rangle$, $\langle d\mu_0/dt\rangle$) for the particle drift paths, the Alfvén boundary can be determined for a given charge, energy, pitch angle, and geomagnetic activity level. This approach has been used to generate similar Alfvén boundary plots by *Liemohn et al.* [1998, 2001]. Figure 3 shows this boundary for 10 eV and 1 keV electrons (specified at geosynchronous orbit) under a Kp = 1 Volland-Stern convection field (see *Jordanova et al.* [1996] for the drift velocities in a shielded Volland-Stern field). The energy and pitch angle dependence is associated with the gradient-curvature drift, which is in the same direction as corotation for electrons. This drift preferentially excludes higher-energy and high pitch angle electrons the inner region. Thus the 10 eV boundary is inward of the 1 keV boundary. It is seen in Figure 3 that the Alfvén boundaries are beyond geosynchronous orbit near dusk but are inside of this altitude at midnight, dawn, and noon. The 10 eV boundary crosses geosynchronous orbit about MLT = 1500 and 2100, while the 1 keV boundary crosses this altitude at about MLT = 1400 and 2200. Both cross the dawn terminator between L = 5 and 6 within 0.5 R_E of each other.

[22] These boundary locations explain many of the features seen in Figure 2. The absence of electrons on the morningside at L = 6 for the all-processes simulation is simply because this location is beyond the Alfvén boundary. The significant energization at L = 5 on the morningside is because this location is just inside of the boundary. It also illustrates that L = 5 electrons at MLT = 0600 came from out near L = 6 at MLT = 0000 and expand back out to L = 6 around MLT = 1200. The radial expansion on the dayside enhances the filling of the trapped zone, explaining the slightly higher flux levels in the all-processes results in the afternoon sector. Electrons resulting from dayside photoionization have uniquely recognizable features on the nightside.

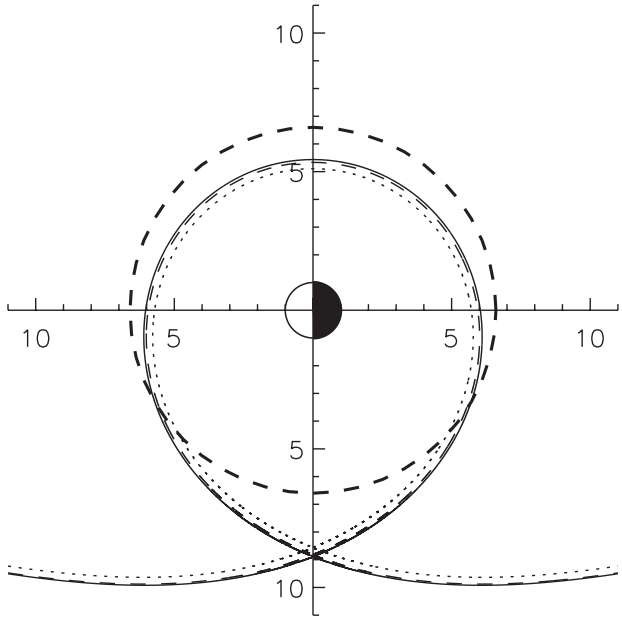

Figure 3. Electron Alfvén boundaries under a Kp = 1 Volland-Stern convection field for [E, α_0] = [10 eV, 90°] (dotted line), [1 keV, 90°] (solid line), and [1 keV, 20°] (dashed line). The dark dashed line is geosynchronous orbit, shown for reference.

[23] It is impractical to show this type of line plot for each pitch angle of interest. Color contour plots are used to show the entire velocity space flux distribution at a chosen location. While some features will be lost in the color scale, this format allows for a more complete presentation of the features in the photoelectron spectra. Figure 4 shows the energy-pitch angle distribution of differential number flux from the dayside photoelectron source at several locations on the nightside. Here (and elsewhere) "pitch angle" refers to equatorial pitch angle, and the pitch angle distribution at any other point along the field line can be easily determined by mapping these values along the field line, taking into account the change in pitch angle due to the magnetic field strength variation (first adiabatic invariant). It is seen in the first row of Figure 4 (L = 3) that the photoelectrons are rapidly depleted across the nightside, particularly at the lowest energies. Corotation dominates at this L shell and therefore very little energization occurs. The second row (L = 4) also shows severe depletion across the nightside magnetosphere. This depletion is entirely from Coulomb energy decay and pitch angle scattering.

[24] At high L shells (last 2 rows of Figure 4) the same effects can be seen in the progression of the distribution around the nightside as at lower L shells, but another process is also affecting the distribution: compression of the flux tubes by the convective electric field. Notice that the fluxes at L = 5 actually increases through the predawn sector. Conversely, the L = 6 fluxes are very small in the predawn sector because this location is outside of the Alfvén boundary for electrons in this energy range. These changes in flux intensity are due to convection (albeit weak) pushing the electrons in from higher L shells, where the distribution was less eroded by collisional processes. In addition, this inward motion of the electrons adiabatically energizes them, further reducing the influence of collisions at degrading this population. The result is that a significant number of photoelectrons can survive the transit through the nightside inner magnetosphere during periods of quiet geomagnetic activity.

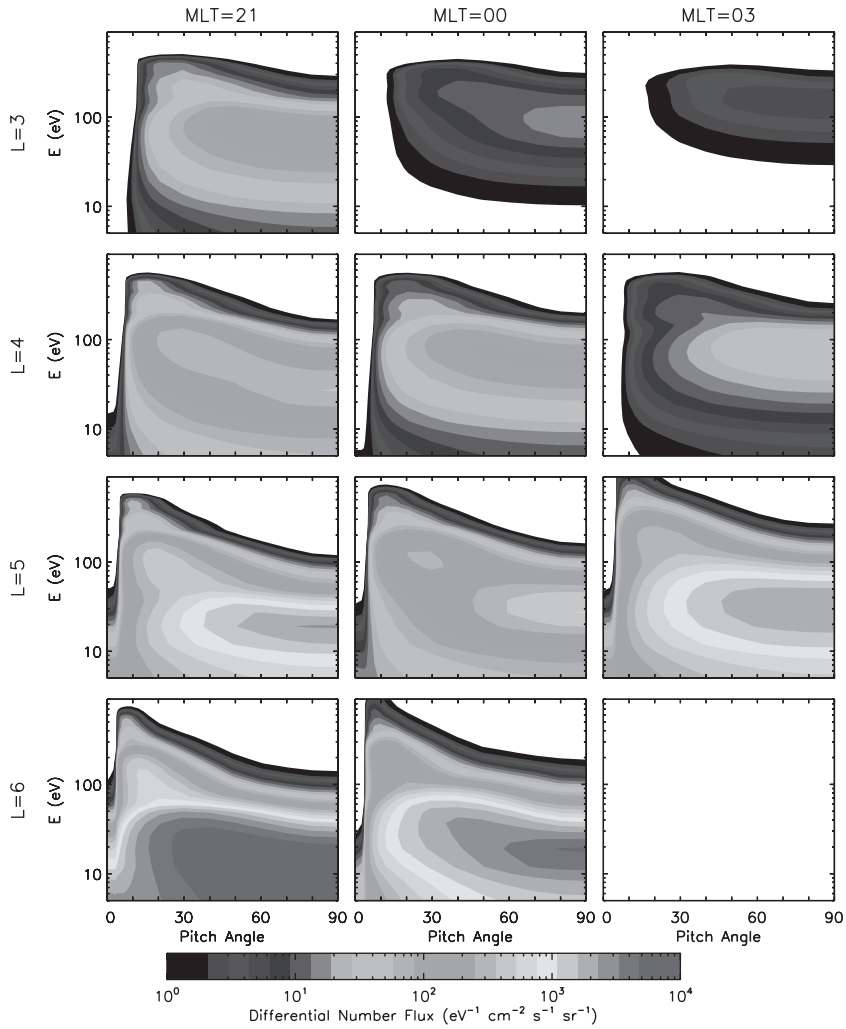

Figure 4. Velocity space flux distributions of the dayside photoelectrons across the nightside inner magnetosphere. The rows are at L = 3 through 6 and the columns are at MLT = 2100, 0000, and 0300. Note that the color scale is logarithmic (as in the other figures). See color version of this figure at back of this issue.

[25] Also, it is interesting to note that the fluxes at L = 5 at MLT = 0000 seem to have two local maxima in the velocity space distribution (these can be seen in other panels of Figure 4, to a much lesser degree). This is from the corresponding maxima in the source cone distribution on the dayside (around 25, 200, 350, and 500 eV). The dayside distributions have ridges at these energies, peaking at the source cone and decreasing through the trapped zone. The extent of these ridges into the trapped zone diminishes with increasing energy. Once these flux tubes are transported to the nightside, the source cone becomes a loss cone, and collisional scattering degrades the flux level in the trapped zone, most prominently at small pitch angles. Thus a peak forms in velocity space somewhere along the ridge. Because the scattering efficiency is a function of energy, the location of this peak shifts to smaller equatorial pitch angles with increasing energy. Thus the peak is near 90° at low energies but is only at 30° at high energies.

[26] These electrons traversing the nightside magnetosphere will have an effect on the superthermal electron distribution on the dayside. Figure 5 shows the electron distribution at two locations on the dayside (L = 5, MLT = 0600 and 1200) to highlight the continued transport of these particles back through the dayside region. Note that the color scale is different from Figure 4 (the same is true for the later figures). The left-hand panels show results from a simulation with all processes included (as in Figure 4), while the right-hand panels show results from a simulation where all of the electrons propagating through the nightside magnetosphere have been removed. At MLT = 0600 (top row), the spectra at 90° equatorial pitch angle exhibits a nightside influence at all energies above a few eV. At angles just inside the trapped zone (5°–20°), the nightside-traversing electrons are significant only at high energies (E > 100 eV), with electrons above the range of the photoelectron source spectrum (509 eV) still clearly present in the distribution. By local noon (bottom row) the influence on the distribution has diminished, but enhanced trapped zone fluxes can still be seen at high pitch angles at energies above ~50 eV. By the afternoon sector this influence is no longer visible in the distribution.

3.2. Scattered Light Photoelectron Source

[27] As mentioned above, a nightside source of photoelectrons exists that has not been examined previously in a global context. The photon spectra from *Strobel et al.* [1974] were used in the single flux tube model to generate a distribution that is applied throughout the loss cone (source cone) pitch angle range in the bounce-averaged model. Figure 6 shows the field line averaged electron energy spectrum from this source (averaged over plasmaspheric altitudes). The spectrum includes not only the primary photoelectrons from the scattered light but also the secondary and

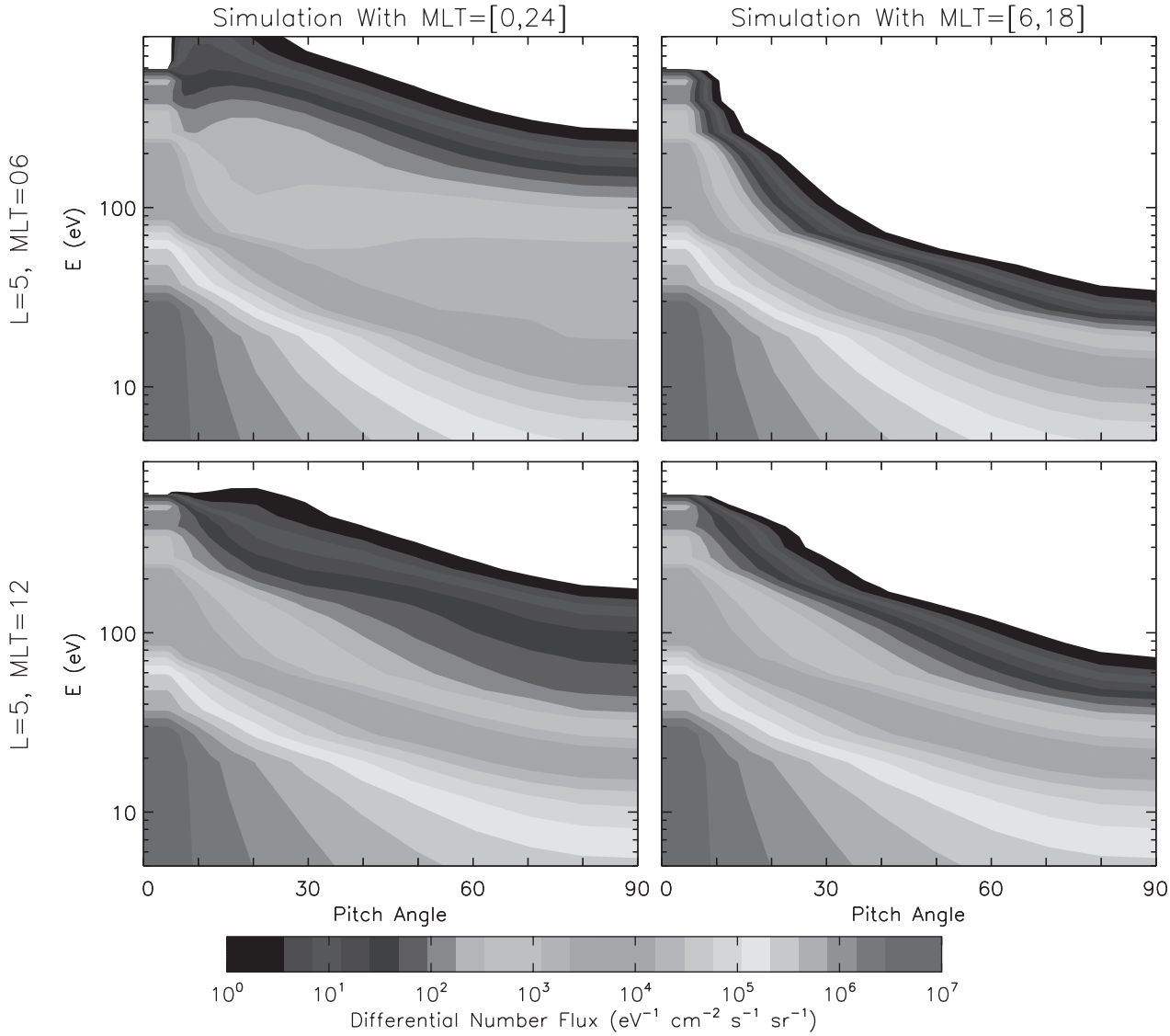

Figure 5. Velocity space flux distributions of the dayside photoelectrons at two locations on the dayside (L = 5, MLT = 0600 and 1200), showing the contribution of the photoelectrons that have traversed the nightside magnetosphere to the dayside distributions. The left column shows results from a simulation including these nightside-propagating electrons, while the right column shows results from a simulation with these electrons artificially omitted. Both simulations include the effects of all physical processes described in the text. See color version of this figure at back of this issue.

tertiary (and so on) electrons generated in the two ionospheric foot points of the flux tube. This is a low-energy population with a sharp cutoff above 28 eV. There are also order of magnitude variations in the flux level, with a deep minimum near 21 eV. The shape of this spectrum is because the primary electrons are created by only a few distinct photon spectral lines, namely, those that resonate with upper atmospheric species (particularly the Lyman α, Lyman β, He I 58.4 nm, and He II 30.4 nm lines). Note that this energy spectrum is much smoother than the photoionization energy spectrum in the ionospheric source region. The fluxes have been averaged along the field line at the loss cone boundary. Electrons have undergone collisional decay and scattering by the upper atmosphere and ionosphere as well as by the plasmaspheric particles. For simplicity, the same distribution is applied at all local times and latitudes (L shells). Therefore, differences in the magnetospheric distribution of these particles is from magnetospheric processes (collisional or drift-induced) rather than from variations in the topside ionospheric electron spectrum. This loss cone boundary condition was generated using the 130° solar zenith angle photon spectra from *Strobel et al.* [1974], taken as an average nighttime electron spectra from this source.

[28] Figure 7 shows the energy-pitch angle distribution at several locations on the nightside magnetosphere from this source. For the most part it has the general features of a source cone distribution with decreasing fluxes at higher pitch angles. This is especially true at the lower L shells. However, L = 5 and 6 display unusual characteristics. As with the dayside photoelectrons, this is because of the weak convection electric field compressing the nightside plasmasphere (which includes these photoelectrons), spatially focusing them and energizing them. The distribution at MLT = 0300 and L = 6 (lower right panel) has an interesting contour plot that should be discussed. Essentially, it has such a unique form because of the interplay between convection and collisional scattering/loss. Collisional scattering tries to fill the trapped zone, but convection pushes these particles inward. In addition, collisional energy degradation further inhibits the largest

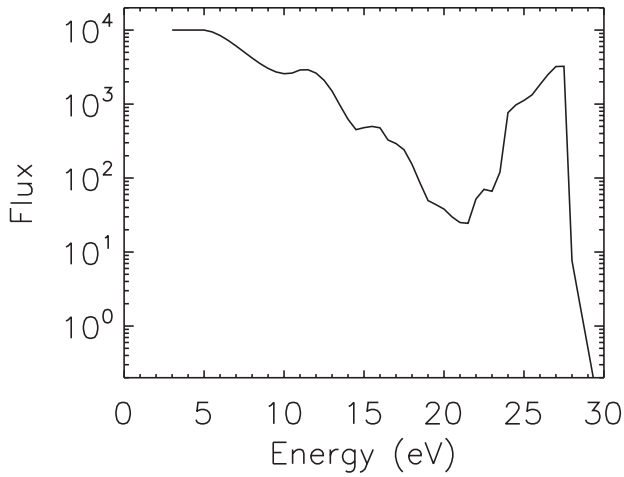

Figure 6. Scattered light photoelectron source cone distribution produced by the single flux tube model for use a boundary condition in the bounce-averaged model. This spectrum is applied (without variation) at all local times and latitudes (L shells) within the simulation domain.

pitch angles from filling. The high-energy tail is from scattering from the peak in the source cone distribution. It angles upward because this energy takes some time to scatter into the trapped zone, during which the particles are energized by the convective compression of the flux tube.

[29] These particles will not have much (if any) effect on the dayside photoelectron velocity space distributions, however. This is because the energy range of the scattered light electrons ($E < 30$ eV, but up to 60 eV with the adiabatic energization on the dawnside) quickly fills in with particles from the dayside source cone, where the intensities are 3 orders of magnitude higher (compare Figures 1 and 6). Therefore it is not necessary to show the progression of these particles through the dayside inner magnetosphere.

3.3. Combined Source

[30] Now that these two sources of photoelectrons have been examined separately, it is useful to show them together to see where each population dominates in velocity space at each spatial location. Figure 8 shows the energy-pitch angle distribution at several locations on the nightside for this combined source population. At low L shells it is clear that the scattered light photoelectrons dominate at low energies and the dayside photoelectrons dominate at high energies. However, neither have partic-

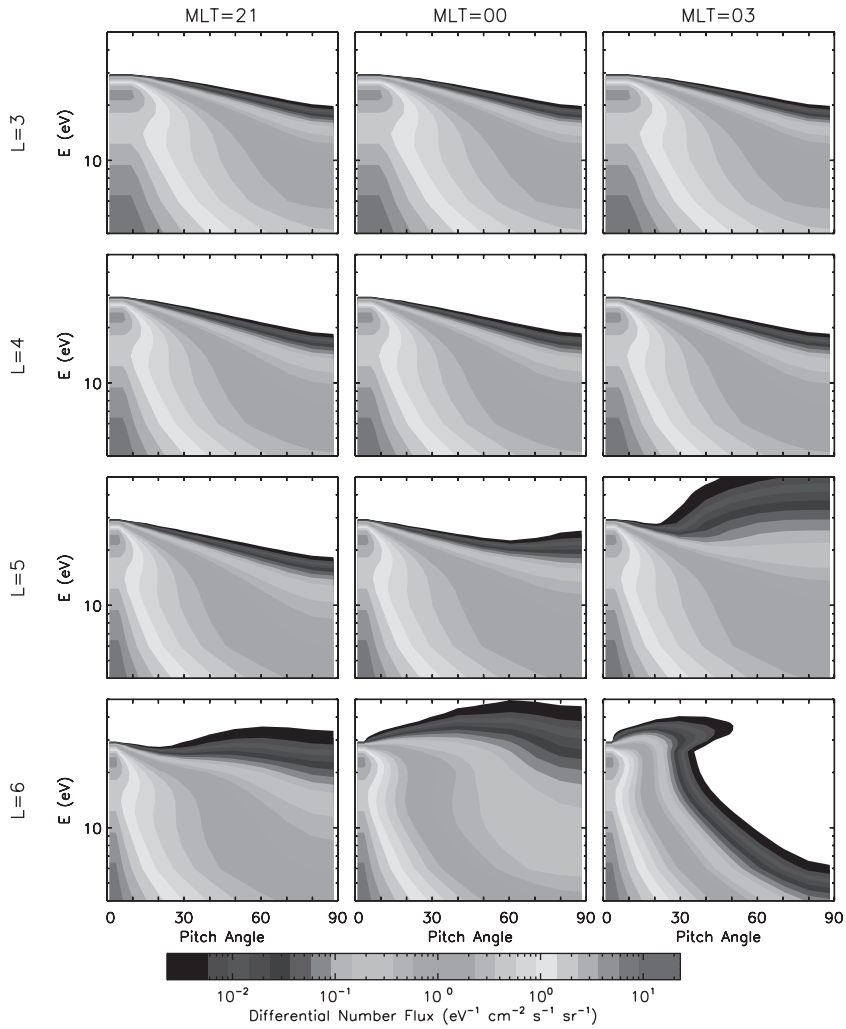

Figure 7. Velocity space flux distributions of the scattered light photoelectrons across the nightside inner magnetosphere. Rows and columns are the same as in Figure 4. See color version of this figure at back of this issue.

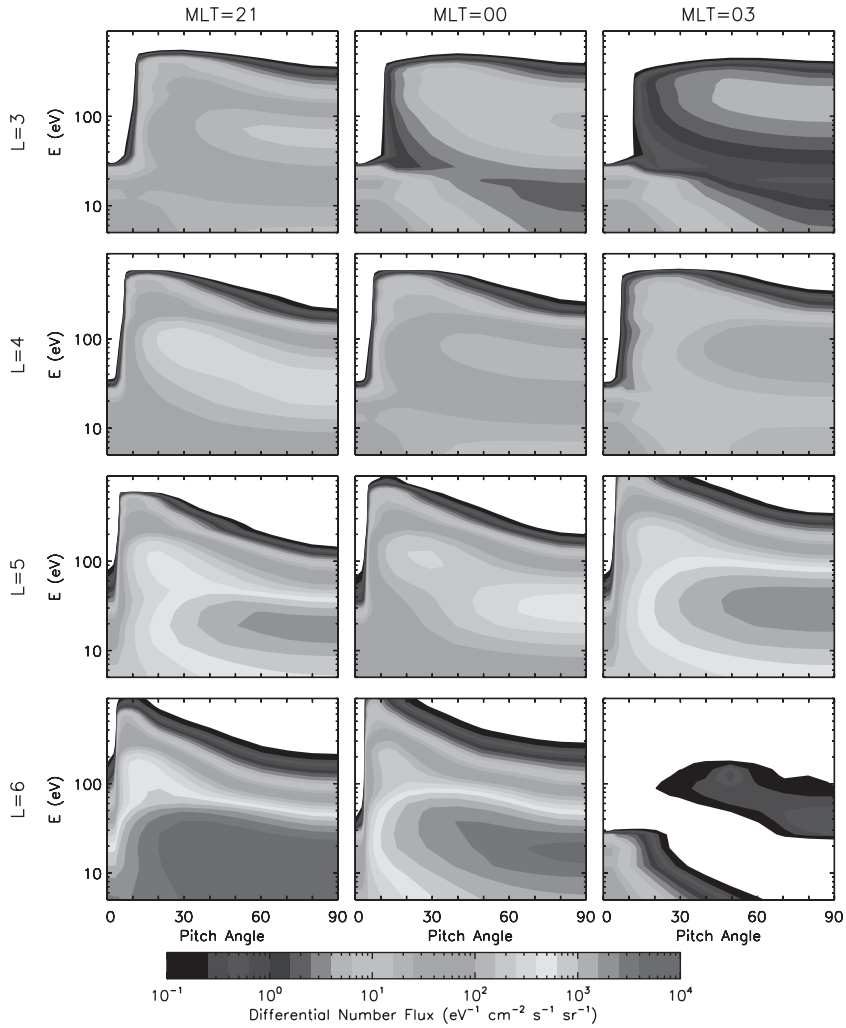

Figure 8. Velocity space flux distributions from both photoelectron sources across the nightside inner magnetosphere. Rows and columns are the same as in Figure 4. See color version of this figure at back of this issue.

ularly large flux levels. In the outer L shells of the nightside plasmasphere it is seen that the dayside photoelectrons dominate over a much larger region of velocity space. The scattered light photoelectrons, though, are still noticable at low energies near the loss cone. At $L = 6$ and MLT = 0300, of course, which is beyond the Alfvén boundary for these electrons, neither source population contributes significantly to the trapped zone flux. This location will be dominated by plasma sheet electrons, which have direct convective access from the near-Earth magnetotail.

[31] A major energy loss mechanism of these electrons is Coulomb degradation through collisions with the thermal plasma. The efficiency of energy transfer from the primary to the target particle is a function of the relative speed between them [see, e.g., *Khazanov et al.*, 1994]. This means that very little energy is transferred to the thermal ions, and most of the heat input is imparted into the thermal electron population. Because of the high conductivity of the thermal electrons, most of this energy will flow down the field line into the ionosphere (where there are far more particles to absorb the energy). So, a convenient quantity that conveys the influence of the superthermal electrons on the thermal plasma is the magnetospheric energy flux into the topside ionosphere resulting from Coulomb energy degradation with the thermal electrons. Figure 9 shows such column heating rates for three local time cuts in the predawn sector, normalized to 800-km altitude. The heating rates from three superthermal electron sources are shown: the dayside photoelectron source, the scattered light photoelectron source, and the plasma sheet electron source. The third population is taken from the results of *Khazanov et al.* [1998] for a steady $Kp = 1$ convection electric field.

[32] Several features are distinctly seen in Figure 9. One is the dominance of the dayside photoelectron source in the outer plasmasphere region at these local times, with energy fluxes up to 10^7 eV cm^{-2} s^{-1} coincident with the peak of the hot electron band through the nightside. Deep in the plasmasphere, the electrons from the scattered light source are the biggest suppliers of energy to the thermal electrons, albeit the heat flux is very small. In the outermost region of the simulation domain the plasma sheet electrons dominate the energy flux. During an injection event where plasma sheet electrons are captured onto closed drift paths inside the plasmasphere (as was simulated by *Liemohn et al.* [1998] and *Khazanov et al.* [1998]), the dayside photoelectrons would disappear from this spatial region and the plasma sheet electrons would dominate the column heating rates throughout most of the nightside inner magnetosphere. However, these captured plasma sheet electrons will only last for a few days in this region, and eventually the profiles seen in Figure 9 would be restored.

[33] Two governing factors in the energy deposition rate are the number densities of the superthermal and thermal electron populations. The energy loss rate is proportional to each of these, so near the source of the superthermal electrons, the heating rate

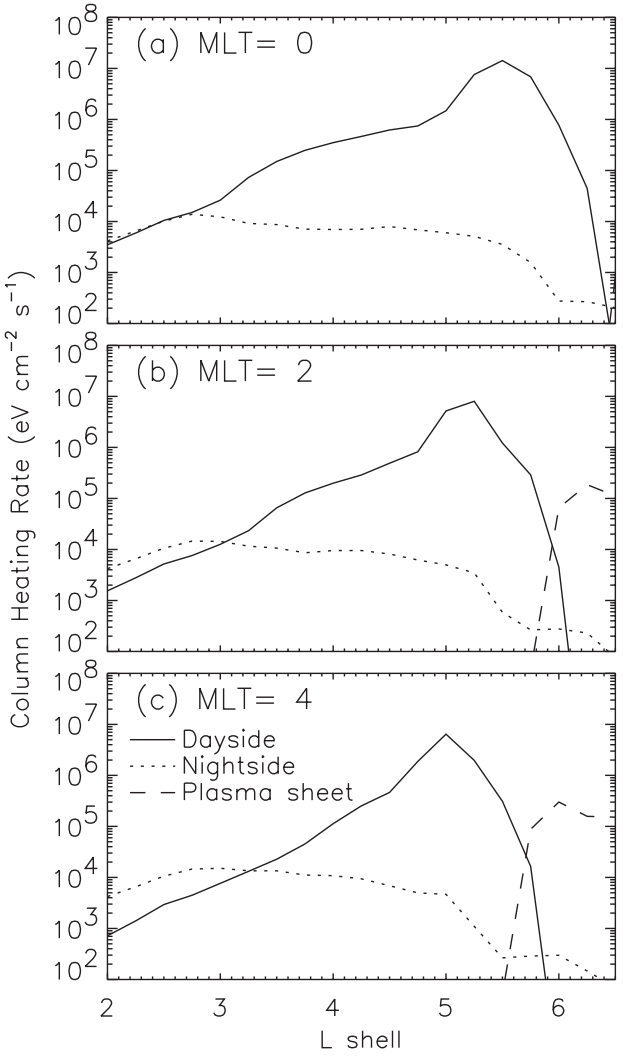

Figure 9. Energy deposition rates to the thermal electrons versus L shell at three predawn magnetic local times from dayside photoelectrons (solid line), scattered light electrons (dotted line), and plasma sheet electrons (dashed line). The heating rates are integrated along the flux tubes and presented at an altitude of 800 km.

increases with both of these quantities. However, far from the superthermal electron source location, the local superthermal electron density depends on the integral content of thermal plasma along the convection path the electrons have traversed. Therefore increasing the thermal plasma density everywhere in the simulation domain could very well decrease the predawn heating rates from the electrons produced by the dayside photon source. Such a global increase in thermal plasma density can be caused by solar cycle phase or by choosing a later time in the plasmaspheric refilling process. For the results shown here the thermal plasma densities have been calculated for the rising phase of the solar cycle (summer 1998) after 4 days of refilling. Such a choice yields nominal thermal plasma densities in the "filled" plasmasphere, and the steady state cold plasma densities could be up to a factor of 2 higher or lower. A detailed parametric study of the effects of the thermal plasma density, especially with respect to solar cycle, season, and convection history, is recommended for a future study.

4. Conclusions

[34] It was shown that photoelectrons created in the dayside ionosphere could traverse the nightside inner magnetosphere when convection is low. Many uniquely recogizable features in the nightside magnetospheric electron distribution are attributable to this flow of photoelectrons from the dayside. A band in space from L = 4 to 6 exists throughout the nightside and morningside magnetosphere, with a distinctive shape in velocity space. In addition, photoelectrons created by light scattered in the upper atmosphere and geocorona fill the trapped zone everywhere on the nightside magnetosphere. They also exhibit the spatial focusing and energization experienced by the dayside source photoelectrons, with distinctive characteristics in their velocity space distribution. The combined source distribution on the nightside is dominated by the scattered light photoelectrons at low L shells and by the dayside photoelectrons at high L shells.

[35] The magnitude of the nightside fluxes from these sources is often well above unity, and in fact approach 10^3 at some locations in phase space (in the chosen differential number flux units of eV^{-1} cm^{-2} s^{-1} sr^{-1}). Such values should be detectable in electron spectrometer observations in the inner magnetosphere. However, the conditions before the measurement must be conducive to the formation of these distributions on the nightside. Namely, it must be geomagnetically quiet for at least 12 hours, and a day or two of extremely quiet conditions would be ideal for the formation of the high-intensity band just inside the plasmapause. Possible sources of observational confirmation of our theoretical predictions are the data sets from the high-altitude plasma instrument on DE 1, the Hydra instrument on Polar, the low-energy plasma analyzer on CRRES, and the magnetospheric plasma analyzer on the geosynchronous satellites operated by the Los Alamos National Laboratory. A survey of the literature did not produce any published nightside inner magnetospheric electron spectra fitting the selection criteria. The search for these populations in the available data sets is a proposed task for consideration.

[36] **Acknowledgments.** This work was supported by National Science Foundation (NSF) grants ATM-9711381, ATM-9710326, and ATM-9800830, and National Aeronautics and Space Administration (NASA) grants NAG5-4771, NAG5-6976, NAG5-5030, and NCC8-181.

[37] Janet G. Luhmann thanks Thomas E. Cravens and Marina Galand for their assistance in evaluating this paper.

References

Bell, K. L., and R. P. Stafford, Photoionization cross sections for atomic oxygen, *Planet. Space Sci.*, *40*, 1419, 1992.

Bilitza, D., Progress report on IRI status, *Adv. Space Res.*, *10*(11), 3, 1990.

Conway, R. R., Photoabsorption and photoionization cross sections: A compilation of recent measurements, *NRL Memo Rep.*, *6155*, 1988.

Fennelly, J. A., and D. G. Torr, Photoionization and photoabsorption cross sections of O, N_2, O_2, and N for aeronomic calculations, *At. Data Nucl. Data Tables*, *51*, 321, 1992.

Fok, M.-C., J. U. Kozyra, A. F. Nagy, C. E. Rasmussen, and G. V. Khazanov, Decay of equatorial ring current ions and associated aeronomical consequences, *J. Geophys. Res.*, *98*, 19,381, 1993.

Fok, M.-C., T. E. Moore, J. U. Kozyra, G. C. Ho, and D. C. Hamilton, Three-dimensional ring current decay model, *J. Geophys. Res.*, *100*, 9619, 1995.

Hedin, A. E., Extension of the MSIS thermospheric model into the middle and lower atmosphere, *J. Geophys. Res.*, *96*, 1159, 1991.

Hinteregger, H. E., K. Fukui, and B. R. Gilson, Observational, reference and model data on solar EUV, from measurement on AE-E, *Geophys. Res. Lett.*, *8*, 1147–1150, 1981.

Jordanova, V. K., et al., October 1995 magnetic cloud and accompanying storm activity: Ring current evolution, *J. Geophys. Res.*, *103*, 79, 1998.

Khazanov, G. V., and G. D. Gefan, The kinetics of ionosphere-plasmasphere transport of superthermal electrons, *Phys. Solariterr.*, *19*, 65, 1982.

Khazanov, G .V., and M. W. Liemohn, Non-steady-state ionosphere-plasmasphere coupling of superthermal electrons, *J. Geophys. Res.*, *100*, 9669, 1995.

Khazanov, G. V., and M. W. Liemohn, Comparison of photoelectron theory against observations, *Geospace Mass and Energy Flow, Geophys. Monogr. Ser.*, vol. 104, edited by J. L. Horwitz, D. L. Gallagher, and W. K. Peterson, p. 333, AGU, Washington, D. C., 1998.

Khazanov, G. V., T. I. Gombosi, A. F. Nagy, and M. A. Koen, Analysis of

the ionosphere-plasmasphere transport of superthermal electrons, 1, Transport in the plasmasphere, *J. Geophys. Res.*, *97*, 16,887, 1992.

Khazanov, G. V., M. W. Liemohn, T. I. Gombosi, and A. F. Nagy, Non-steady-state transport of superthermal electrons in the plasmasphere, *Geophys. Res. Lett.*, *20*, 2821, 1993.

Khazanov, G. V., T. Neubert, and G. D. Gefan, Kinetic theory of ionosphere plasmasphere transport of suprathermal electrons, *IEEE Trans. Plasma Sci.*, *22*, 187, 1994.

Khazanov, G. V., T. E. Moore, M. W. Liemohn, V. K. Jordanova, and M.-C. Fok, Global, collisional model of high-energy photoelectrons, *Geophys. Res. Lett.*, *23*, 331, 1996.

Khazanov, G. V., M. W. Liemohn, J. U. Kozyra, and T. E. Moore, Inner magnetospheric superthermal electron transport: Photoelectron and plasma sheet electron sources, *J. Geophys. Res.*, *103*, 23,485, 1998.

Khazanov, G. V., M. W. Liemohn, J. U. Kozyra, and D. L. Gallagher, Global energy deposition to the topside ionosphere from superthermal electrons, *J. Atmos. Solar Terr. Physics*, *62*, 947, 2000.

Lejeune, G., ''Two stream'' photoelectron distributions with interhemispheric coupling: A mixing of analytical and numerical methods, *Planet. Space Sci.*, *27*, 561, 1979.

Liemohn, M. W., and G. V. Khazanov, Non-steady-state coupling processes in superthermal electron transport, in *Cross-Scale Coupling in Space Plasmas, Geophys. Monogr. Ser.*, vol. 93, edited by J. L. Horwitz, N. Singh, and J. L. Burch, p. 181, AGU, Washington, D. C., 1995.

Liemohn, M. W., G. V. Khazanov, T. E. Moore, and S. M. Guiter, Self-consistent superthermal electron effects on plasmaspheric refilling, *J. Geophys. Res.*, *102*, 7523, 1997a.

Liemohn, M. W., G. V. Khazanov, and J. U. Kozyra, Guided plasmaspheric hiss interactions with superthermal electrons, 1, Resonance curves and timescales, *J. Geophys. Res.*, *102*, 11,619, 1997b.

Liemohn, M. W., G. V. Khazanov, and J. U. Kozyra, Banded electron structure formation in the inner magnetosphere, *Geophys. Res. Lett.*, *25*, 877, 1998.

Liemohn, M. W., J. U. Kozyra, M. F. Thomsen, J. L. Roeder, G. Lu, J. E. Borovsky, and T. E. Cayton, Dominant role of the asymmetric ring current in producing the stormtime *Dst**, *J. Geophys. Res.*, *106*, 10,883, 2001.

Mantas, G. P., H. C. Carlson, and V. B. Wickwar, Photoelectron flux build-up in the plasmasphere, *J. Geophys. Res.*, *83*, 1, 1978.

Maynard, N. C., and A. J. Chen, Isolated cold plasma regions: Observations and their relation to possible production mechanisms, *J. Geophys. Res.*, *80*, 1009, 1975.

Polyakov, V. M., G. V. Khazanov, and M. A. Koen, The ionosphere-plasmasphere photoelectron transport, *Phys. Solariterr.*, *10*, 93, 1979.

Rasmussen, C. E., S. M. Guiter, and S. G. Thomas, Two-dimensional model of the plasmasphere: Refilling time constants, *Planet. Space Sci.*, *41*, 35, 1993.

Solomon, S. C., P. B. Hays, and V. J. Abreu, The auroral 6300 Å emission: Observations and modeling, *J. Geophys. Res.*, *93*, 9867, 1988.

Stern, D. P., The motion of a proton in the equatorial magnetosphere, *J. Geophys. Res.*, *80*, 595, 1975.

Strobel, D. F., T. R. Young, R. R. Meier, T. P. Coffey, and A. W. Ali, The nighttime ionosphere: *E* region and lower *F* region, *J. Geophys. Res.*, *79*, 3171, 1974.

Volland, H., A semiempirical model of large-scale magnetospheric electric fields, *J. Geophys. Res.*, *78*, 171, 1973.

G. V. Khazanov, National Space Science and Technology Center, NASA Marshall Space Flight Center, Huntsville, AL 35812, USA.

M. W. Liemohn, Space Physics Research Laboratory, University of Michigan, 2455 Hayward Street, Ann Arbor, MI 48109-2143, USA. (liemohn@umich.edu)

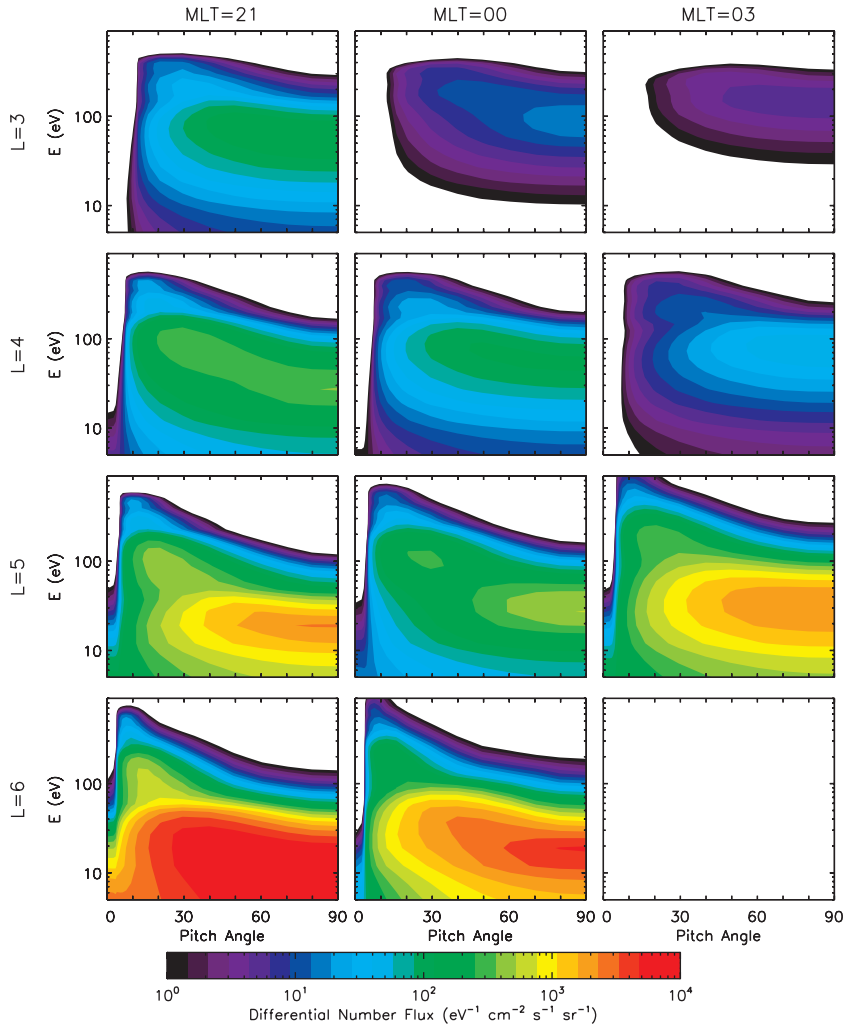

Figure 4. Velocity space flux distributions of the dayside photoelectrons across the nightside inner magnetosphere. The rows are at L = 3 through 6 and the columns are at MLT = 2100, 0000, and 0300. Note that the color scale is logarithmic (as in the other figures).

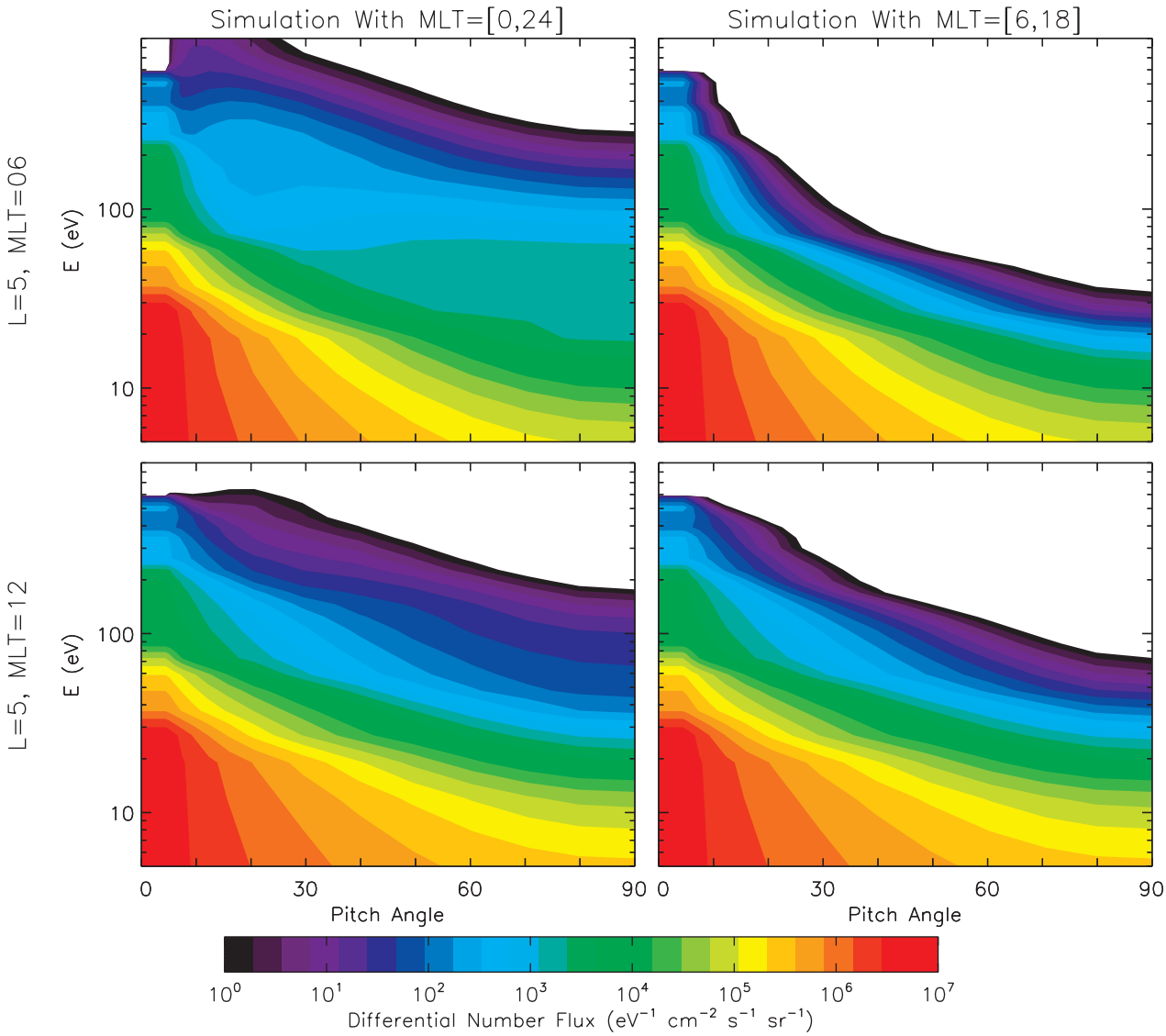

Figure 5. Velocity space flux distributions of the dayside photoelectrons at two locations on the dayside (L = 5, MLT = 0600 and 1200), showing the contribution of the photoelectrons that have traversed the nightside magnetosphere to the dayside distributions. The left column shows results from a simulation including these nightside-propagating electrons, while the right column shows results from a simulation with these electrons artificially omitted. Both simulations include the effects of all physical processes described in the text.

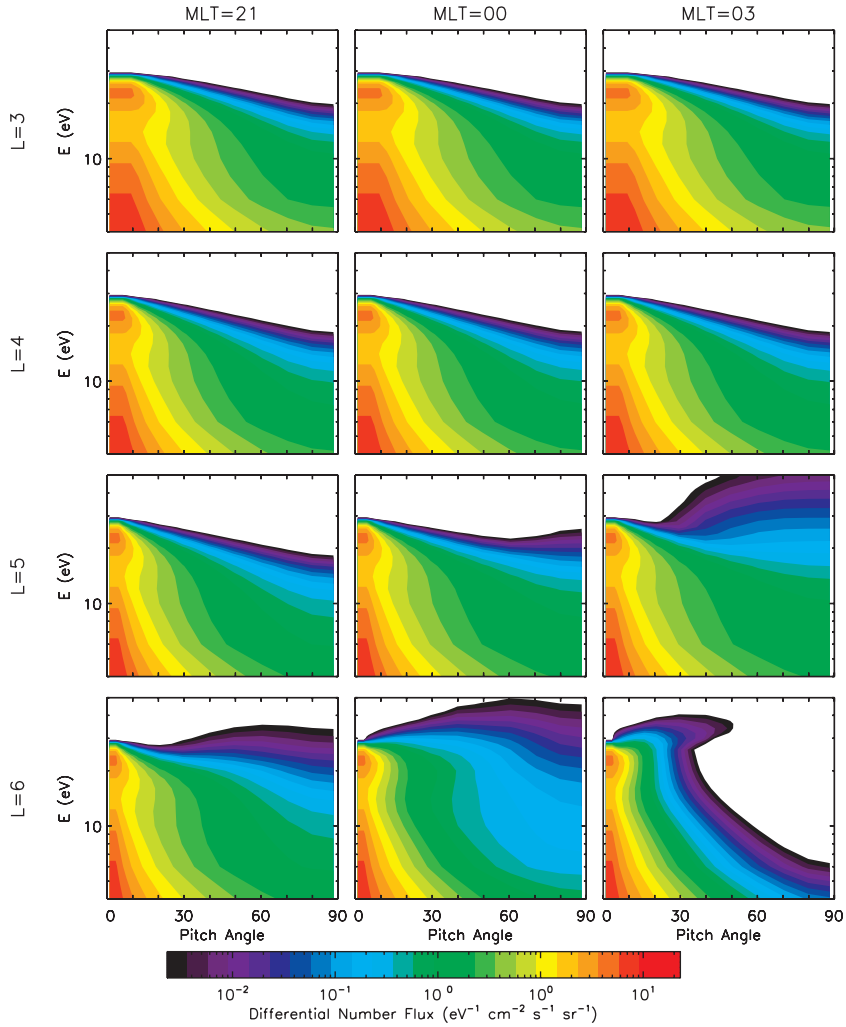

Figure 7. Velocity space flux distributions of the scattered light photoelectrons across the nightside inner magnetosphere. Rows and columns are the same as in Figure 4.

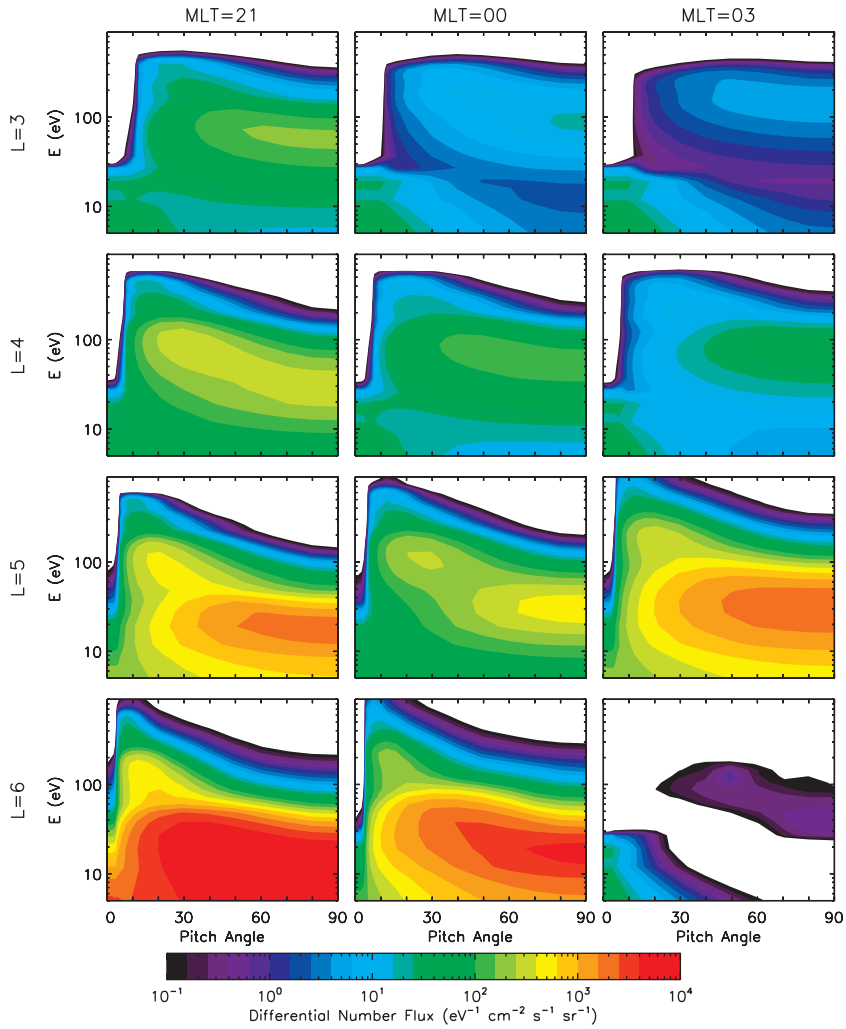

Figure 8. Velocity space flux distributions from both photoelectron sources across the nightside inner magnetosphere. Rows and columns are the same as in Figure 4.